Improving Organic Photovoltaic Efficiency via Heterophase Homojunction Copper Indium Sulfide Nanocrystals

*Zhonglin Du, Ting Yu, Wanting He, Aycan Yurtsever, Ricardo Izquierdo, and Dongling Ma**

Eco-friendly heterophase homojunction copper indium sulfide quantum dots (HH-CIS QDs) terminated by short hydroxyl ligands are integrated into non-fullerene organic solar cells (OSCs) for the first time. Experimental results exhibit that this novel nanostructure can improve sunlight absorption and charge transfer ability, harvesting more photons and converting them to charge carriers. Additionally, the formation of hydrogen bonds between 2-mercaptoethanol-capped HH-CIS QDs and the interface modification layer is beneficial for better interfacial contact, which promotes work function modification, reduces surface roughness, and increases interfacial charge transfer. Benefiting from HH-CIS QDs incorporation, nonfullerene OSCs involving two different types of photoactive layers and three different types of electron transport layers all demonstrate improved photoelectric conversion efficiency (PCE). With QDs concentration optimization, nonfullerene OSCs with the PM6:ITIC-4F and PM6:Y6 absorbers exhibit excellent PCEs of 14.04% and 16.26%, respectively. As compared to those reported previously, HH-CIS QDs into the interface between the electron charge layer and photoactive layer lead to significant performance improvement, with both achieve PCEs and enhancement factors among the highest ones reported for various QD-integrated OSCs. The results strongly suggest that the rational design of QDs and their optimal integration are critical for performance enhancement.

Z. Du, T. Yu, W. He, A. Yurtsever, D. Ma
Institut National de la Recherche Scientifique (INRS)
Centre Énergie Materiaux et Télécommunications
Varennes, Québec J3X 1P7, Canada
E-mail: ma@emt.inrs.ca

Z. Du
College of Materials Science and Engineering
The National Base of International Science and Technology
Cooperation on Hybrid Materials
Qingdao University
Qingdao 266071, P. R. China

R. Izquierdo
Département de Génie Électrique
École de Technologie Supérieure
Montréal, Québec H3C 1K3, Canada

The ORCID identification number(s) for the author(s) of this article can be found under https://doi.org/10.1002/solr.202300320.

1. Introduction

The urgent demand for high-efficiency and low-cost photovoltaic devices is constantly driving the development of solar cells. Nonfullerene organic solar cells (OSCs) are currently considered the most promising organic solar cells to be commercialized in the short-term period. Significant efforts have been made to improve their photovoltaic performance with a record power conversion efficiency (PCE) value of over 19%.[1] Gaining a high efficiency and long-term stability of these devices remains an important task for realizing widespread industrial applications. Introducing an additional component is still a simple and efficient strategy to enhance both PCEs and device stability.[2] Currently, various additional components have been integrated into OSCs, which play different roles in improving device performance.

Colloidal quantum dots (QDs) exhibit tunable photophysical properties depending on their size, shape, composition, ligands, and surrounding environments.[3,4] The most attractive feature is their tunable bandgaps that can be tailored to modulate their absorption wavelengths from ultraviolet (UV), visible (vis), to near-infrared (NIR) regions, which is useful for solar energy utilization. To date, diverse colloidal QDs have been incorporated into OSCs in different ways, and their contribution to device performance varies with how they are integrated.[5–12] Generally, QDs' integration into OSCs has the following four major effects: 1) harvesting more photons or optimizing the film morphology by blending the colloidal QDs into the photoactive layer directly;[7,9–14] 2) enhancing charge carriers extraction and transfer by incorporating the QDs into the electron transport layers or hole transport layers (ETLs/HTLs);[15] 3) modifying the interface between the photoactive layer and charge transport layer, and thus reducing the interfacial charge recombination by introducing the colloidal QDs as interfacial modifiers;[6,8,16–20] and 4) improving the device stability of the OSCs by suppressing the aggregation and possible oxidation of photoactive materials either by direct QD blending with the photoactive layer or by depositing a separate, robust QD passivation layer.[7] In the past, type-I core/shell QDs such as CdSe/ZnS, PbS/CdS, and CuInS$_2$/ZnS have been extensively employed to improve the efficiency of

OSCs, mainly by enhancing the exciton generation and dissociation through the fluorescence resonance energy transfer (FRET) effect between the photoactive materials and QDs.[8,11,12] Performance enhancement can also be realized through the charge separation at the interface of QDs and photoactive materials due to the appropriate energy-level alignment.[21] However, the wider bandgap of shell materials of the QDs can suppress the charge transfer from the core of the QDs to other QDs and materials in the photoactive layer of solar cells and therefore does not contribute to increased charge carrier collection of solar cells. In contrast, type-II nanostructured QDs, such as ZnTe/CdSe and CdTe/CdSe, exhibit better charge separation and transfer ability due to their energy band alignment of the core and shell materials, which is important for application in solar cells.[22,23] However, the majority of such core/shell QDs produced by the heteroepitaxial growth process easily cause interface traps and energy band shifts due to the lattice mismatch of different materials.[24–26] Type-II heterophase homojunction nanocrystals emerge as excellent candidates for solving the above problems.[27–29] Heterophase homojunction nanocrystals are composed of different crystalline structures of core and shell materials of the same chemical composition, which have slightly different energy levels, allowing the effective separation of electrons and holes and thereby their extraction. Nonetheless, the synthesis of type-II heterophase homojunction nanocrystals is highly challenging for most semiconductor materials. $CuInS_2$ (CIS) QDs are an attractive less-toxic alternative to Cd- or Pb-based QDs. They also stand out with high absorption coefficient ($\approx 10^5$ cm^{-1}), the direct bandgap of 1.5 eV (bulk bandgap energy), and widely tunable spectral wavelengths from visible to NIR. All these features make CIS QDs excellent candidates for sunlight harvesting applications.

Besides, the interparticle transport of charge carriers among the QDs and the interfacial charge transport between QDs and the organic material play a critical role in the optoelectronic performance of solar cells. The surface ligands of QDs particularly influence the charge transfer efficiency of the photogenerated carriers. In the typical synthesis process of QDs, the long alkyl chains, such as oleic acid, oleylamine, trioctylphosphine, and trioctylphosphine oxide, are usually selected to control the QDs growth and ensure their monodisperse and stability. However, due to their insulating properties, the charge transport process can be hindered or even completely blocked. Therefore, to meet the application requirements in OSCs, it is necessary to improve the charge transport performance of QDs through the ligand exchange process.

Herein, a novel type-II heterophase homojunction nanostructure based on the eco-friendly CIS QDs has been successfully developed, revealing the controllable absorption and emission ranges.[30,31] These rationally prepared heterophase homojunction CIS (HH-CIS) QDs were then cast on the surface of the photoactive absorber layer, leading to enhanced efficiency in nonfullerene OSCs. In particular, they contributed to the performance by broadening the absorption range of solar cells to the NIR region and by allowing effective charge separation and extraction owing to their type-II homojunction structure. Meanwhile, the long carbon chain on the surface of HH-CIS QDs was replaced by a short ligand of 2-mercaptoethanol (ME) to form a hydroxyl-terminated surface chemical structure,

which can increase the interfacial contact between the photoactive layer and charge transport layer, and reduce morphological defects at the interface, thereby increasing the electron transfer from photoactive layer to electrode. Thanks to the synergistic effect of the above positive contributions arising from the interfacial incorporation of ME-capped HH-CIS QDs, the PCEs approached 14.04% for the PM6:ITIC-4F-based OSCs and 16.26% for the PM6:Y6-based OSCs, respectively.

2. Results and Discussion

The type-II HH-CIS QDs were synthesized through a two-step injection procedure using an approach modified from the literature.[30] The core CIS QDs were first synthesized at low temperature. The corresponding transmission electron microscopy (TEM) image is shown in Figure S1, Supporting Information. The size of the core CIS QDs is about 3 nm. As shown in Figure S2, Supporting Information, the light absorption edge is about 600 nm, which corresponds to a bandgap of 2.14 eV, consistent with the reported result.[30] **Figure 1** shows the TEM image of monodispersed HH-CIS QDs. The statistical size distribution of the core–shell QDs obtained from TEM images showed a mean diameter of about 7.8 ± 0.8 nm (Figure S3, Supporting Information). Lattice fringes of the HH-CIS QDs can be observed clearly in the high-resolution TEM (HR-TEM) image, and the lattice fringe spacing of 0.314 nm is consistent with the interplanar spacing of the hexagonal wurtzite shell. However, the spacings corresponding to the core cubic chalcopyrite QDs could not be readily resolved in Figure 1b. The inset in Figure 1b shows the fast Fourier transform (FFT) obtained from the HR-TEM image of the same QD and resembles the diffraction pattern from the (100) zone axis of the shell wurtzite phase CIS. Furthermore, the inverse FFT of the HH-CIS QDs shown in Figure 1c can clearly distinguish the nanostructure contribution of core and shell from the diffraction pattern. To further investigate the crystalline structure, XRD of the CIS core and HH-CIS QDs was measured, as shown in Figure S4, Supporting Information. The XRD pattern of the CIS core QDs shows a characteristic diffraction peak around 19°, which belongs to the cubic chalcopyrite structure (JCPDS 85-1575). Other diffraction peaks at 27°, 48°, and 54° were broad because of the small size of CIS core QDs. The XRD pattern of HH-CIS QDs is dramatically different from that of CIS core, showing characteristic diffractions of the wurtzite phase, indicative of the formation of the wurtzite shell. It was also noticed that the diffraction peaks of HH-CIS QDs became sharp, which suggests improved crystallinity during the shell formation process.[30] The crystalline structure of the HH-CIS QDs was also characterized by selected area electron diffraction (SAED). As shown in Figure S5, Supporting Information, the SAED patterns of HH-CIS QDs can be indexed into the (312) and (204) plans of the cubic chalcopyrite phase of the core CIS QDs, as well as the (002), (110), and (112) crystal planes of the wurtzite phase of the shell, which is consistent with XRD results. Figure S6, Supporting Information displays the UV–vis absorption and PL emission spectra of HH-CIS QDs with different shell thicknesses. The shell thickness of the prepared QDs was varied by tuning the volume ratio of the added core QDs to shell precursors.
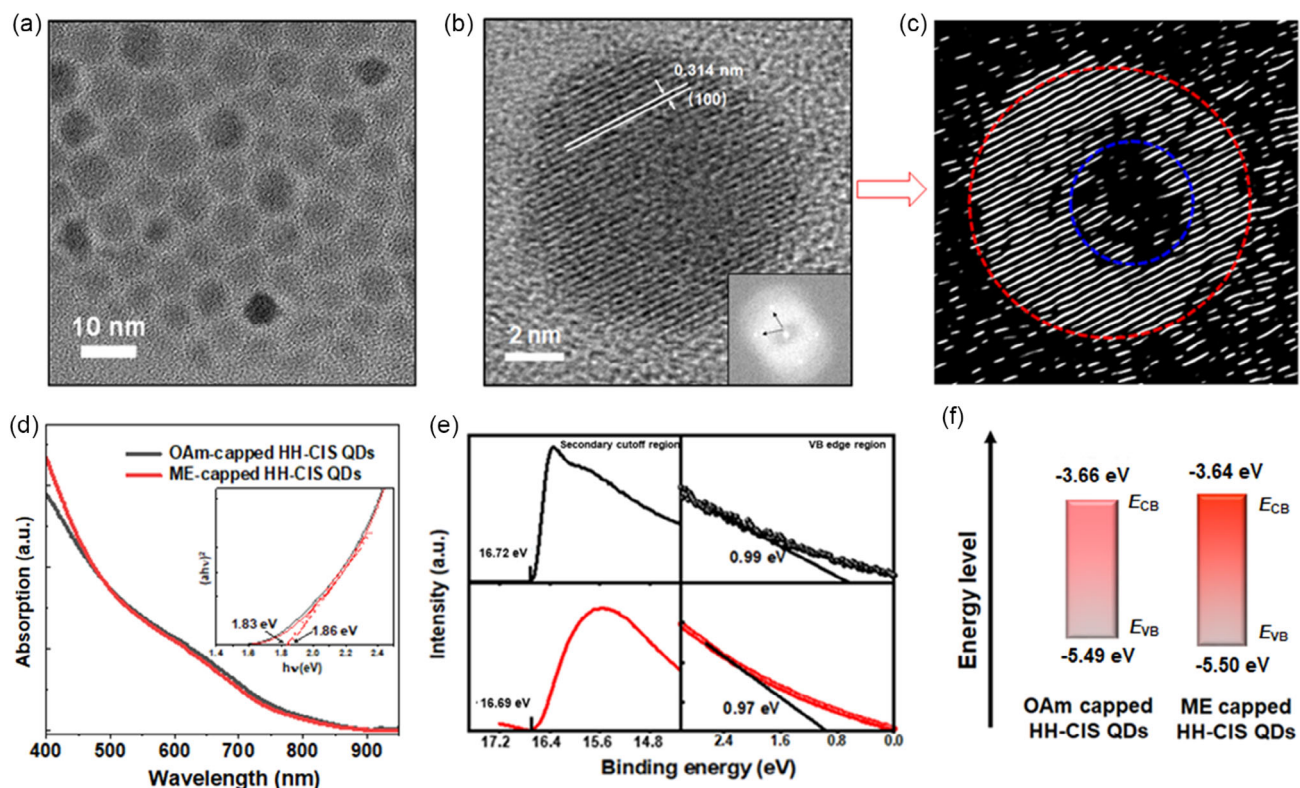
Figure 1. a) TEM and b) HR-TEM images of the HH-CIS QDs; the inset in (b) is FFT of the HH-CIS QDs; c) inverse FFT of the HH-CIS QDs. Characterization of OAm- and ME-capped HH-CIS QDs: d) UV–vis absorption spectra of OAm- and ME-capped HH-CIS QDs, e) UPS spectra of secondary electron cutoff and valence band of ME- and OAm-capped HH-CIS QDs, and f) schematic illustration of the energy levels with respect to the vacuum level (E_{vac}).

Along with the increase in shell thickness, both the absorption and emission spectra exhibited a redshift. The significant redshifts of absorption and emission spectra are typical characteristics for type-II core/shell QDs, confirming the core–shell QD formation. Meanwhile, PL dynamics were also studied to further explore the optical properties of the HH-CIS QDs. The PL decay curves of the HH-CIS QDs with three different shell thicknesses are exhibited in Figure S6b, Supporting Information. The PL intensity of the core CIS QD was so weak that its PL decay signal could not be obtained. The average PL lifetime (τ_{ave}) values were calculated using the biexponential decay fitting $I_{PL}(t) = a_1 e^{-t/\tau_1} + a_2 e^{-t/\tau_2}$, where a_1 and a_2 are fractional contributions of PL decay lifetimes, and τ_1 and τ_2 are different lifetime components, respectively. The detailed decay data are listed in Table S1, Supporting Information. The τ_{ave} value, measured at the PL peak wavelength, increased from 120.24 to 295.12 ns with the increase of shell thickness, which further supports the formation of the type-II structure of HH-CIS QDs.[30,32,33] Therefore, with the increase of the shell thickness of the HH-CIS QDs, the photogenerated electrons and holes could have larger spatial separation and thus promoting the charge transfer to other QDs or semiconductor materials in solar cells.[27]

As the typical QDs were synthesized with the assistance of insulating long alkyl chains, which could hinder or even block the charge transport process in optoelectronic devices, ligand exchange with shorter ones must be done. Additionally, it is known that for the layer-by-layer fabrication of OSCs, a solvent compatible with already-deposited layer materials can cause film damage to the previously deposited layers. Taking this into consideration, we thought that it was better to avoid nonpolar organic solvents for the QD layer deposition to eliminate the film damage issue. Based on these two considerations, a short-chain ME ligand was selected to replace the long OAm chain via the ligand exchange process. The short-chain ME ligand can enhance the charge transport between adjacent QDs and between the QDs and the photoactive layer. Another merit of the ME ligand is that it enables the HH-CIS QDs to be well dispersed in the polar alcohol solvent, which could then be further deposited on the photoactive layer without any damage to already deposited layers. We carried out FTIR measurements of the HH-CIS QDs before and after the short ligand ME exchange to examine the outcome of ligand exchange (Figure S7, Supporting Information). Compared to the OAm-capped structure, the FTIR spectrum of ME-capped HH-CIS QDs displays the characteristic peaks at 1290, 1232, and 1167 cm^{-1} related to C–H bending vibrations, C–O stretching vibrations, and –OH in-plane vibrations of ME ligand, indicating the successful capping of QDs surface by ME ligands. However, the characteristic peaks of the OAm ligand at 2852 and 2920 cm^{-1}, related to the asymmetric and symmetric C–H stretching modes, could still be detected implying that complete ligand exchange is challenging.

As shown in Figure 1d, the absorption spectra of HH-CIS QD dispersions are not much affected by the ligand exchange process and exhibit a similar absorption onset. The optical bandgaps (E_g) were determined by the Tauc plots according to the equation of $(\alpha h\nu)^2 = (h\nu - E_g)^{1/2}$ where α is the absorption coefficient and $h\nu$ is the photon energy. The E_g values for the HH-CIS QDs capped with OAm and ME ligands were found to be ≈1.83 and 1.86 eV, respectively. We then measured the energy levels of QD films composed of these HH-CIS QDs via UPS measurements. The obtained secondary electron cutoff and valence band regions are shown in Figure 1e and the related parameters are listed in Table S2, Supporting Information. The energy values of the valence band maximum (E_{VB}) of HH-CIS QDs capped with OAm and ME ligands were estimated to be 5.49 and 5.50 eV, respectively, based on the difference between incident light energy (21.22 eV) and the UPS widths (15.73 and 15.72 eV,

respectively) from the secondary cutoff and valence band edge regions. By combing those values of E_{VB} with above measured optical bandgaps (E_g), the energy values of conduction band minimum (E_{CB}) were calculated to be −3.66 eV for OAm-capped and −3.64 eV for ME-capped HH-CIS QDs (Figure 1f). It was noted that the energy level was slightly changed with the ligand exchange process.

After we ascertained the structure of ME-capped HH-CIS QDs, we then integrated them into nonfullerene OSCs with a device configuration of ITO/PEDOT:PSS/PM6:ITIC-4F/QDs/PDINN/Ag (**Figure 2**a), where PM6:ITIC-4F photoactive layer was selected due to its excellent photovoltaic performance. ME-capped HH-CIS QDs were dispersed in methanol and then spin-coated on top of photoactive layer. The concentration of the as-prepared ME-HH-CIS QDs was about 0.32 mg mL^{-1} based on the NAA measurements. Figure 2b exhibits the corresponding
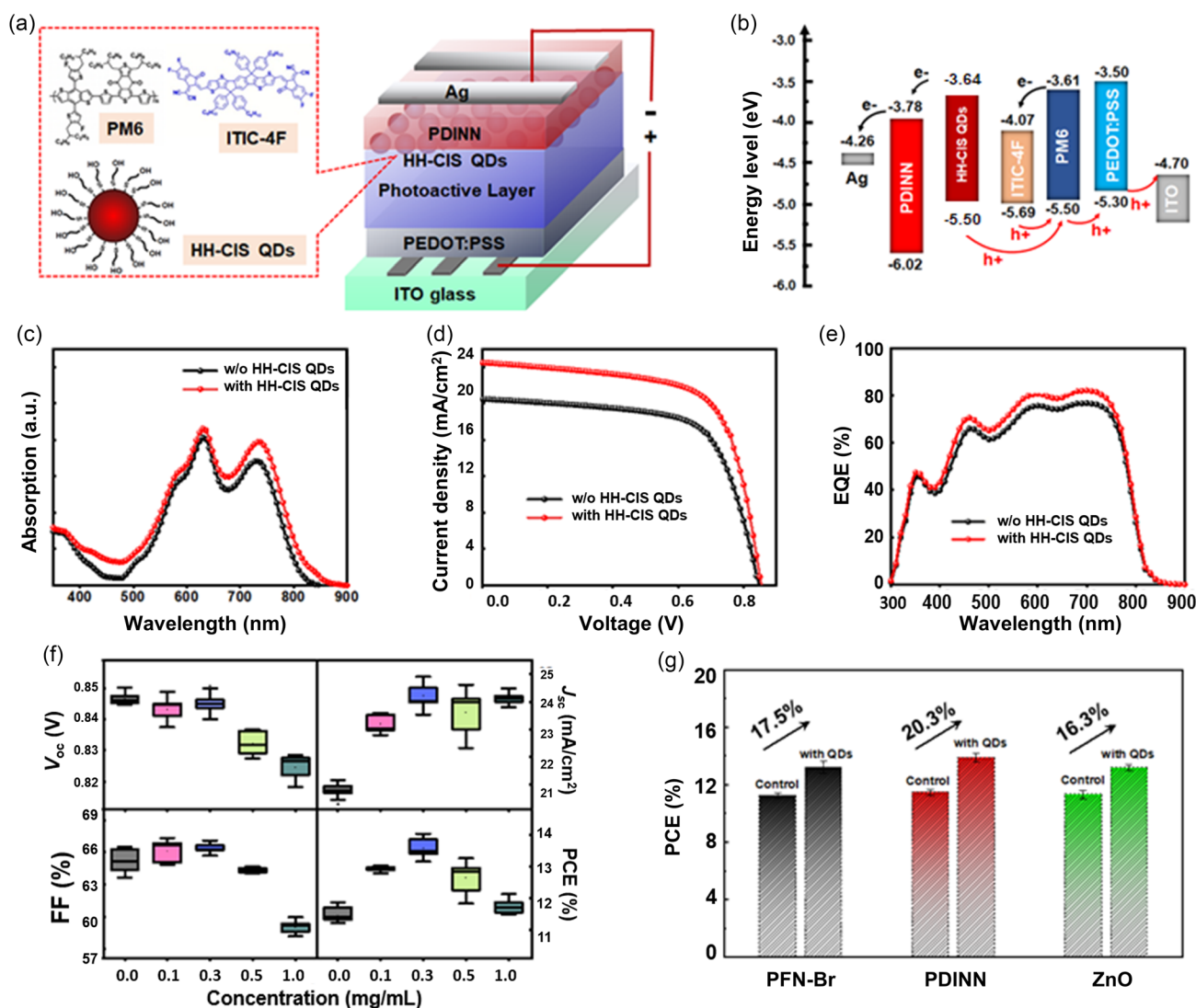
Figure 2. a) Schematic image of HH-CIS QD-integrated nonfullerene OSCs; b) energy levels diagram of the PM6:ITIC-4F device; c) UV–vis absorption spectra of the photoactive PM6:ITIC-4F layers with and without HH-CIS QDs; d) J–V curves; e) EQE curves of the PM6:ITIC-4F devices with and without HH-CIS QDs; f) statistical photovoltaic parameters obtained from ten devices based on different concentrations of QDs; and g) PCE of the HH-CIS QD-integrated PM6:ITIC-4F devices with different electron transport layers.

band energy levels diagram of the QD-incorporated OSCs and proposed charge transfer pathways. Under illumination conditions, the excitons generate from the organic absorbers and then diffuse to the interface between donor and acceptor where they can dissociate into free charge carriers. Finally, the charge carriers diffuse to appropriate electrodes through the interfacial layers (ETL and HTL). At the same time, the generated electrons from the ME-capped HH-CIS QDs inject into the PDINN layer, and the holes transfer into organic donors due to the suitable energy-level alignment between them, which allowed harvesting more photons and increased the possibility of photogenerated charges. Figure 2c shows the UV–vis absorption spectra of the photoactive layer with and without QDs. The UV–vis absorption spectrum of QD-integrated photoactive layer displays absorption peaks at 630 and 734 nm, similar to those of the pristine photoactive layer. But its absorption intensity, especially in the NIR region between 700 and 800 nm, was enhanced. The current density versus voltage (J–V) curves of the ME-HH-CIS QD-incorporated devices and the control device (i.e., without QDs) are shown in Figure 2d, and the photovoltaic parameters are listed in **Table 1**. It could be found that ME-HH-CIS QD-based devices displayed an average PCE of 13.74% ($J_{sc} = 24.08$ mA cm^{-2} $V_{oc} = 0.85$ V, FF $= 67.02\%$), which was considerably higher than 11.61% of the control device ($J_{sc} = 20.45$ mA cm^{-2} $V_{oc} = 0.85$ V, FF $= 67.09\%$). The highest PCE reached 14.04%. The improvement in PCE was mainly attributed to the increase in J_{sc}, ascribing to the effective sunlight capture of HH-CIS QDs (especially in NIR region from 700 to 800 nm) and quite likely also to the enhancement of carriers transport process from QDs to ETL. Furthermore, the variation of the external quantum efficiency (EQE) curve with the integration of the HH-CIS QDs, shown in Figure 2e, matches well with the enhanced absorption in the NIR region due to the HH-CIS QDs deposition. The integrated current density amounts to 22.76 mA cm^{-2}, similar to that obtained from the J–V curves. Besides, the photovoltaic bandgap energy was estimated to be 1.54 eV by identifying the inflection point of the EQE spectrum, i.e., the maximum in the EQE first derivative.[34]

The QDs concentration was also optimized to achieve the best device performance. The statistical photovoltaic parameters are displayed in Figure 2f, and the detailed parameters are listed in Table S3, Supporting Information. We found that with the increase in QDs concentration, all three photovoltaic parameters were initially increased and then decreased. The optimized concentration of QDs solution was found to be ≈0.3 mg mL^{-1}.

Then, devices of ITO/PDINN/Ag and ITO/QD/PDINN/Ag structures were fabricated to understand the influence of HH-CIS QDs on the electrical conductivity across the interface. As shown in Figure S8, Supporting Information, the linear fitted J–V curve showed a very good ohmic contact between the interlayer and electrode regardless of the use of ME-CS CIS QDs. The electrical conductivity can be defined as $\sigma = G_0 \times d_0/S$, where σ is the electrical conductivity, G_0 is the conductance related to the slope of the J–V curve, d_0 is the thickness of QDs/PDINN thin films measured by a profilometer, and S is the device area. In our experiments, d_0 and S values were about 20 nm and 0.06 cm^2 respectively. Thus, σ values were calculated to be 1.01×10^{-4} and 7.22×10^{-5} S cm^{-1} for the HH-CIS QDs (0.3 mg mL^{-1})-incorporated and control devices, respectively. The enhancement of σ value indicates a lower resistance after HH-CIS QDs incorporation, contributing to the charge transfer and extraction. The influence of different QDs concentrations on the electrical conductivities of devices was also investigated and the detailed results are shown in Figure S9 and Table S4, Supporting Information. The incorporation of QDs solution with ≈0.3 mg mL^{-1} concentration provided the best electrical conductivity, which was in line with its highest photovoltaic performance discussed above. It was probably due to the homogenous distribution of HH-CIS QDs on the surface of the photoactive layer. In contrast, the lower concentration could not offer enough interface contact with the photoactive layer, while the higher concentration could easily cause the agglomeration of QDs and poor interfacial contact with the electrode, thus suppressing the charge transport and collection.

Apart from the PDINN ETL, we also investigated the effect of the QDs on the performance of two other structures, using PFN-Br and ZnO layers as ETLs, to demonstrate the universality of our QDs integration approach. The PCEs of the resultant HH-CIS QD-integrated devices with different ETLs are displayed in Figure 2g and the detailed photovoltaic parameters are listed in Table S5, Supporting Information. The PCE of the devices with the PDINN, PFN-Br, and ZnO as the ETLs increased from 11.64% to 14.04%, from 11.21% to 13.21%, and from 11.32% to 13.17%, with an enhancement factor of 20.3%, 17.5%, and 16.3%, respectively, thanks to the QDs integration.

Inspired by these results and to pursue higher PCEs, we moved forward to introduce our HH-CIS QDs into the PM6:Y6-based photoactive system, which has recently reported higher PCE than other nonfullerene OSCs. The J–V curves of the champion devices with and without HH-CIS QDs are shown

Table 1. Effect of HH-CIS QDs on the photovoltaic performance parameters from J–V curves measured under simulated AM1.5G, 100 mW cm^{-2}.

Photoactive layer	Configuration	V_{oc} [V]	J_{sc} [mA cm^{-2}]	FF [%]	PCE [%][a]
PM6:ITIC-4 F	Control	0.85 (0.85 ± 0.003)	20.63 (20.45 ± 0.14)	66.47 (67.09 ± 0.78)	11.64 (11.61 ± 0.05)
	With HH-CIS QDs	0.85 (0.85 ± 0.006)	24.50 (24.08 ± 0.26)	67.10 (67.02 ± 0.43)	14.04 (13.74 ± 0.18)
PM6:Y6	Control	0.83 (0.83 ± 0.002)	24.29 (24.13 ± 0.16)	70.97 (70.24 ± 0.44)	15.17 (15.04 ± 0.11)
	With HH-CIS QDs	0.84 (0.84 ± 0.003)	27.41 26.53 ± 0.31	70.62 70.33 ± 0.68	16.26 (15.98 ± 0.23)

[a]The maximum and average values (in brackets) were obtained from ten devices.

in Figure S10, Supporting Information. The PCE was improved from 15.17% to 16.26% with the HH-CIS QDs integration. These results further demonstrated the generally beneficial contribution of the HH-CIS QDs to nonfullerene OSCs. To highlight the high performance of HH-CIS QD-integrated nonfullerene OSCs, the summary of the previously reported different types of QDs, their integration location, efficiency variations, and major enhancement mechanisms is shown in Table S6, Supporting Information. As compared with the literature data, it can be seen that integrating the eco-friendly HH-CIS QDs into the interface between the ETL and nonfullerene photoactive layer led to significant performance improvement, with both PCEs and enhancement factors among the highest ones reported for QD-integrated OSCs. It strongly suggests that the rational design of the QDs and further their optimal integration are critical for enhancing the performance of solar cells. Besides, the obtained efficiencies based on integrating these eco-friendly HH-CIS QDs are comparable to those of high-toxicity and instable $CsPbI_3$ perovskite QD-incorporated OSCs.

In the following, we focused on the PM6:ITIC-4F system to gain a deeper understanding of the beneficial contribution of the QDs to photovoltaic performance. Notably, PDINN is a very common interfacial modification layer between the photoactive layer and metal electrode, due to its suitable dipole moment and secondary amine in the side chains. To investigate the interfacial contact between the PM6:ITIC-4F-based photoactive layer and PDINN layer after HH-CIS QDs deposition, AFM measurements were carried out. AFM topography images of the photoactive layer before and after the deposition of the HH-CIS QDs are shown in **Figure 3**a,b. The pristine and HH-CIS QD-integrated photoactive layers had a similar fiber-like surface structure. Besides, the HH-CIS QD-integrated photoactive layer film possessed a slightly lower surface roughness, with a root-mean-square (RMS) value of 2.13 nm, than the pristine one (2.45 nm), which indicates that the HH-CIS QDs deposition herein did not cause any photoactive layer damage. We believe it was due to avoiding the use of nonpolar solvents (e.g., toluene) for deposition, thanks to the successful ligand replacement by hydroxyl ME ligands that allowed the use of a polar solvent for the QD deposition. The HH-CIS QD deposition also reduced the possible morphological defects because the well-dispersed small QDs could fill into the small holes or cracks on the surface of the photoactive layer, which explains the reduced roughness of the QDs film. The AFM topography images of the photoactive layer/QDs/PDINN and photoactive layer/PDINN were also measured and are shown in Figure 3c,d. Similarly, the RMS roughness value of the photoactive layer /QDs/PDINN film was smaller than that of the one for the photoactive layer /PDINN film, benefiting from a smoother photoactive layer after the ME-capped HH-CIS QDs deposition. Therefore, the incorporation of
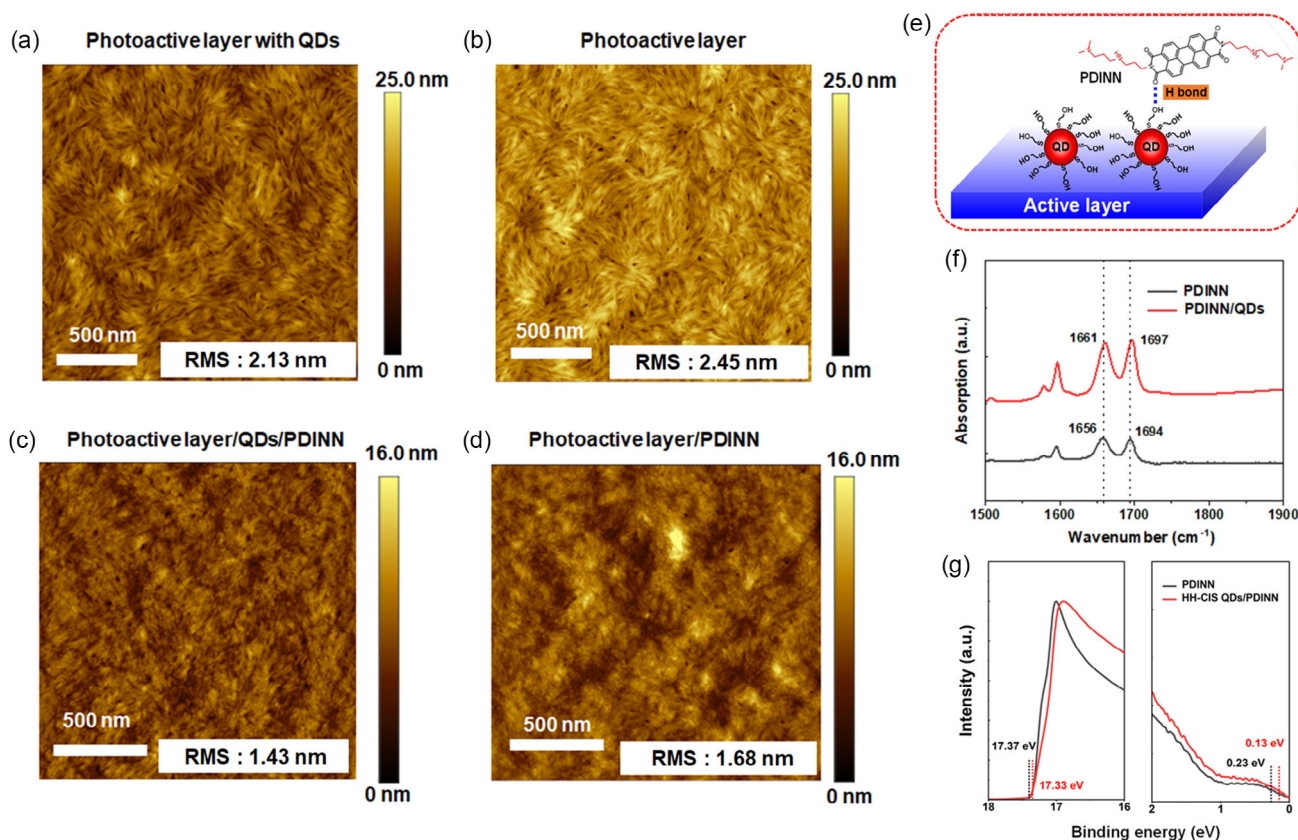

Figure 3. AFM topography images of different films: a) photoactive layer/QDs, b) photoactive layer, c) photoactive layer/QDs/PDINN, and d) photoactive layer/PDINN. Images sizes are 2.0 μm × 2.0 μm. e) Scheme of the possible hydrogen bonds between PDINN and HH-CIS QDs. f) FTIR spectra of PDINN film with and without HH QDs, respectively. g) UPS spectra of the photoactive layer /PDINN films with and without HH-CIS QDs.

ME-HH-CIS QDs can potentially promote the interfacial contact between the photoactive layer and PDINN as well as the contact between the PDINN and Ag electrode, thus resulting in more effective charge transport.

In addition, the good interface contact may be caused by the formation of hydrogen bonding between the OH group of hydroxyl-terminated HH-CIS QDs and the $C=O$ group of PDINN molecules (Figure 3e). To verify the existence of hydrogen bonds, FTIR was carried out on the PDINN films with and without HH-CIS QDs, respectively. As shown in Figure 3f, the characteristic vibrational peaks of $C=O$ at 1656 and 1694 cm^{-1} shifted to 1661 and 1697 cm^{-1}, respectively, for the PDINN/HH-CIS QDs sample, indicating the formation of hydrogen bonds.[35] To further investigate the influence of HH-CIS QDs on the PDINN interface modification layer, UPS was conducted to detect the work function change of PDINN films. The pristine PDINN and QD-modified PDINN films were spin-coated on the surface of photoactive layers. The UPS spectra of the PDINN and HH-CIS QDs/PDINN are displayed in Figure 3g, and the extracted parameters are listed in Table S7, Supporting Information. The values of the secondary E_{cutoff} of PDINN and HH-CIS QDs/PDINN were 17.37 and 17.33 eV, respectively. Generally, the corresponding work function φ could be estimated by the difference between the E_{cutoff} and E_{Fermi} according to the equation $h\nu - \varphi = E_{Fermi} - E_{cutoff}$. The h$\nu$ of incident light energy was 21.22 eV. The values of E_{Fermi} were calculated by the energy difference between the incident light and the Fermi edge (first E_{cutoff}). The values of E_{Fermi} were 20.99 eV for the pristine PDINN and 21.09 eV for the HH-CIS

QD-modified PDINN. Therefore, the work function φ value of PDINN decreased from 4.08 to 4.02 eV with the HH-CIS QD integration. The decrease in the work function of PDINN indirectly supported its surface modification by the HH-CIS QDs, which could accelerate the charge transport from the photoactive layer to the metal electrode.[8]

The charge recombination behavior of the PM6:ITIC-4F-based devices was explored by measuring J_{sc} and V_{oc} as a function of the light intensity (P_{light}) (**Figure 4**a,b). The relationship between J_{sc} and P_{light} was analyzed to assess the bimolecular recombination in OSCs according to the relationship of $J_{sc} \propto (P_{light})^{\alpha}$, where α value describes the bimolecular recombination degree (Figure 4a). When the α value is closer to 1, it means that the device has weaker bimolecular recombination that is beneficial for solar cell performance. The control device without any QDs showed an α value of 0.94, while the device incorporated with the HH-CIS QDs showed a slightly higher value of 0.98, indicating less bimolecular recombination. Differently, V_{oc} correlates to the light intensity by the equation, $V_{oc} = (akT/q) \ln(P_{light})$, where V_{oc} is proportional to $\ln P_{light}$, with the slope related to kT/q, where a is an ideality factor, k is the Boltzmann's constant, q refers to the elementary charge, and T is the tested temperature. The further the slope is close to $1 kT/q$, the less the trap-assisted recombination is. As shown in Figure 4b, the slope of $0.97 kT/q$ for the HH-CIS QD-incorporated device was closer to $1 kT/q$ than that of the control device having a slope of $1.09 kT/q$, which suggests that the HH-CIS QDs incorporation could suppress the trap-assisted recombination in line with a smoother film morphology
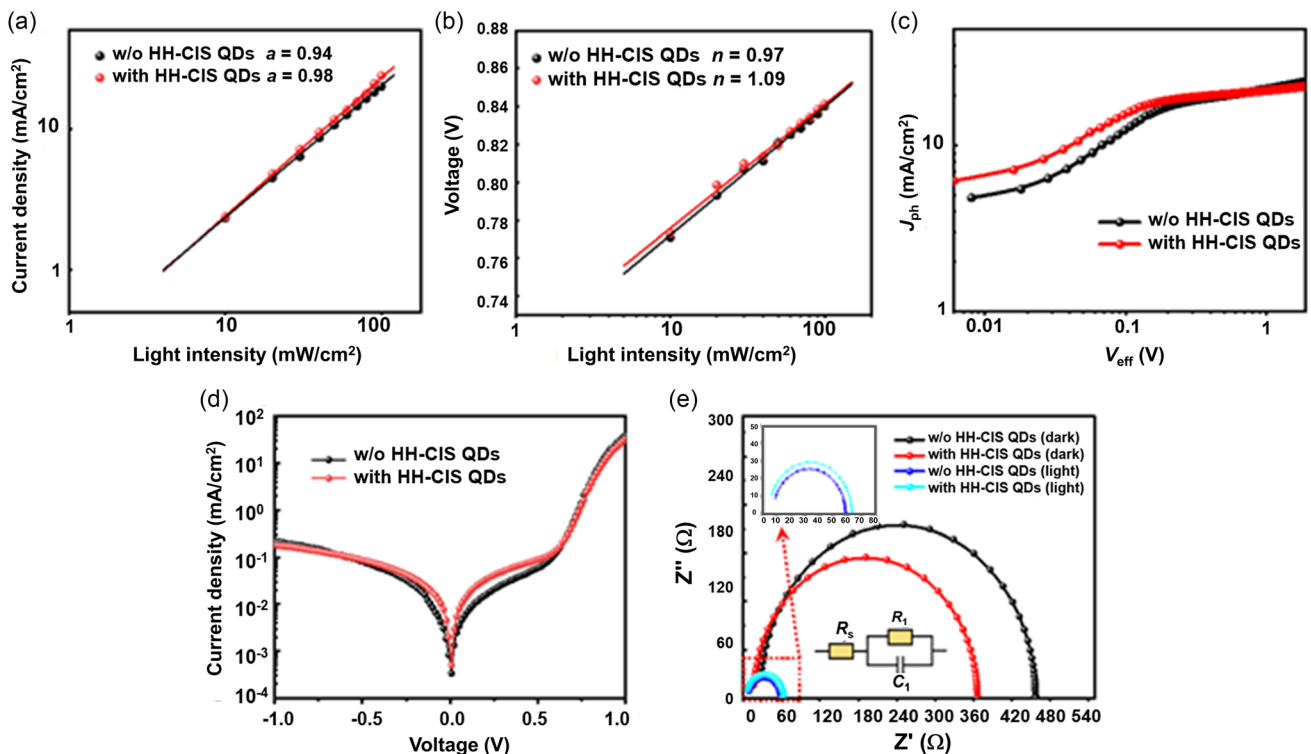
Figure 4. a) J_{sc} versus P_{light}, b) V_{oc} versus P_{light}, c) J_{ph} versus V_{eff}, d) dark current versus voltage, and e) EIS spectra of the solar cells with (red and sky-blue curves) and without (black and blue curves) HH-CIS QDs, respectively. The equivalent circuit model is shown as the inset in (e).

evidenced by AFM measurements (Figure 3a,c). Photocurrent density (J_{ph}) versus effective voltage (V_{eff}) was measured to figure out the exciton dissociation behavior of the nonfullerene OSCs (Figure 4c). At the high reverse bias voltage, J_{ph} is saturated, suggesting the dissociation of almost all the photogenerated excitons to free charge carriers. J_{ph}/J_{sat} represents the possibility of exciton dissociation under short-circuit conditions. J_{ph}/J_{sat} for the PM6:ITIC-4F-based devices without and with HH-CIS QDs were 94.8% and 98.5%, respectively. Thus QD-based device showed considerably more efficient exciton dissociation and charge extraction, leading to a higher J_{sc}. Figure 4d represents the dark $J–V$ curves of the devices with and without HH-CIS QDs to investigate the leakage current. The lower dark current for the HH-CIS QD-based device suggested the suppressed charge recombination from the interface between the photoactive layer and electrodes.[36]

To further explore the difference in charge-transfer dynamics caused by the QD integration, the electrochemical impedance spectroscopy (EIS) measurements were carried out in a frequency range from 1 MHz to 0.1 Hz. Figure 4e exhibits the Nyquist plots of the OSCs with and without the HH-CIS QDs under dark and illumination conditions. The corresponding simulation circuit used for fitting EIS data is also shown in Figure 4e. The fitting parameters of the equivalent circuit are summarized in Table S8, Supporting Information. Herein, R_s is the series resistance related to the metallic wires and electrodes, while R_1 is the charge recombination resistance, and C_1 stands for the chemical capacitance in the device. No matter whether under dark and illumination conditions, the R_s values of the HH-CIS QD-integrated devices are much lower than those of the control ones. Under dark conditions, the R_1 value of the HH-CIS-based device was lower (350.2 $\Omega\,cm^2$) than that of the control one (431.4 $\Omega\,cm^2$), indicating that the HH-CIS QDs can efficiently suppress the charge recombination and accelerate the charge transfer process. While under sunlight illumination, the charge recombination resistance R_1 of the HH-CIS QD-integrated device was similar (58.9 $\Omega\,cm^2$) to the control one (51.5 $\Omega\,cm^2$), but much lower than those under dark conditions, again in agreement with the reduced charge recombination, which further explained the higher FF and PCE of the HH-CIS QD-integrated device.[37–40]

Considering the beneficial effect of the ME-HH-CIS QDs on electrical conductivity, the carrier mobility of devices was studied by the SCLC method. As shown in **Figure 5** and Table S9, Supporting Information, the electron and hole mobilities of devices (μ_e and μ_h) increased from 6.92×10^{-5} to $1.88 \times 10^{-4}\ cm^2\,V^{-1}\,s^{-1}$ and from 1.97×10^{-4} to $3.32 \times 10^{-4}\ cm^2\,V^{-1}\,s^{-1}$ after being modified with HH-CIS QDs, respectively. In addition, more balanced charge carrier mobility ($\mu_h/\mu_e = 1.78$) was achieved by the HH-CIS QDs incorporation, which is attributed to more photogenerated carriers and less charge recombination at the interface, thereby leading to a higher J_{sc}.

To study the effect of the optical absorption of HH-CIS QDs on the device performance of solar cells, we modeled and calculated the sunlight absorption of each layer in the devices with and without the QDs using the transfer matrix method (TMM).[41–43] The TMM can provide a powerful prediction for the light path and absorption inside a device structure. The optical field distribution in the OSCs with the structure of ITO (100 nm)/PEDOT:PSS (20 nm)/photoactive layer (120 nm)/PDINN (5 nm)/Ag (100 nm) with and without QDs was simulated by TMM. For simplicity, the heterophase homojunction structure of HH-CIS QDs was only considered as the bulk structure, which served as a thin layer of about ($\approx$10 nm) on the surface of the photoactive layer. The n index of the photoactive layer and QDs was obtained according to the reported literature.[44,45] As depicted in **Figure 6**a–d, the optical field distribution in the PM6:ITIC-4F and PM6:Ya6-based OSCs with and without QDs was first simulated under the irradiation of the standard sunlight. The interference fringes can be observed in the image of optical field distribution, induced by interference between the incident light, and reflected light from the Ag electrode. As shown in the simulated optical field distribution images, the light absorption intensity of both the PM6:ITIC-4F and PM6:Y6-based devices with the HH-CIS QDs layer is much higher than the pristine one, especially in the visible region. Meanwhile, as depicted in Figure 6e–h, the photogenerated exciton distribution in the photoactive layer can be calculated according to the optical field distribution and absorption coefficient of the photoactive layer. The exciton generation rate in the photoactive layer can be estimated according to the equation: $\rho(\lambda) \propto |E(\lambda)|^2/h\nu \ast \alpha(\lambda)$; among them, $\rho(\lambda)$ is the exciton generation rate, $|E(\lambda)|^2$ is the optical field intensity, and $\alpha(\lambda)$ is the absorption coefficient. The values of calculated photogenerated exciton density at the interface between
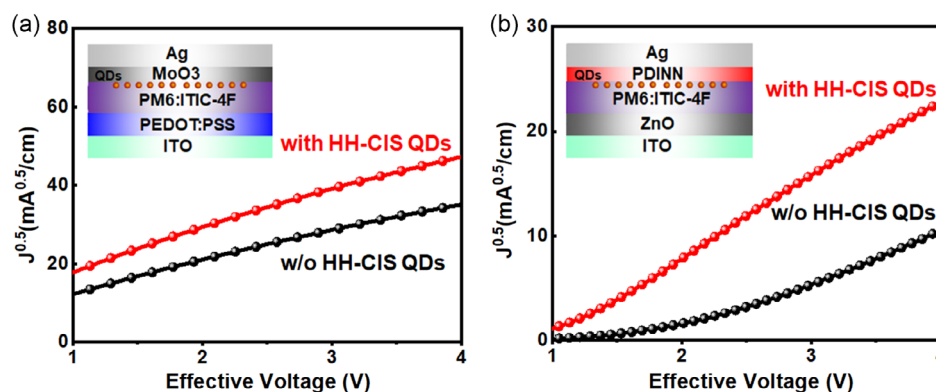
Figure 5. a) The structure of hole-only SCLC diodes and hole mobility of the devices with and without HH-CIS QDs, and b) the structure of electron-only SCLC diodes and electron mobility of the devices with and without HH-CIS QDs.
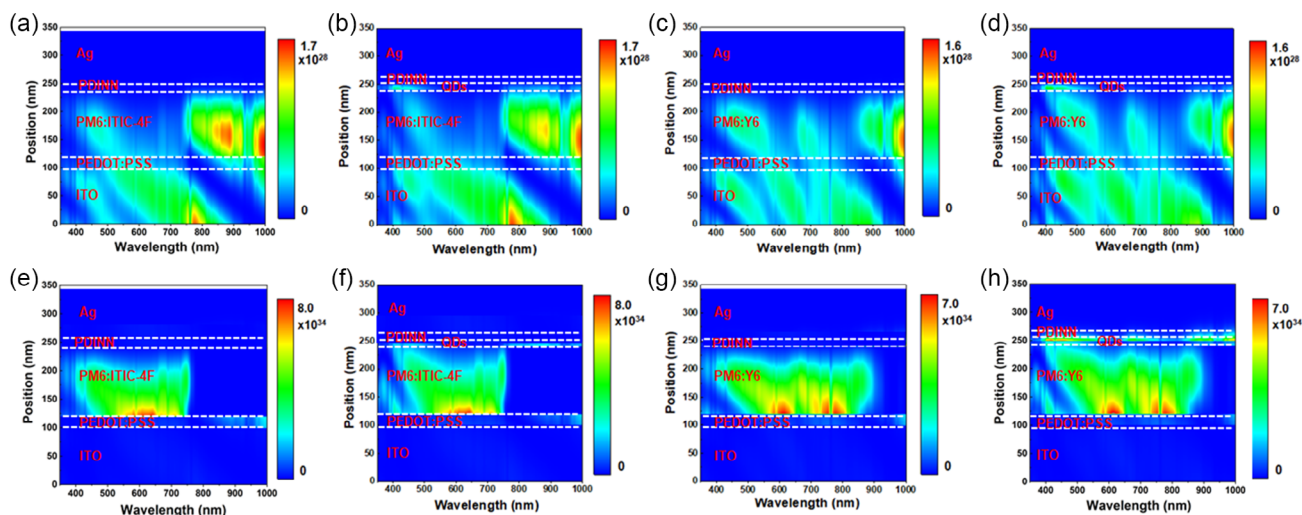
Figure 6. The simulated optical field distribution in the photoactive layer of PM6:ITIC-4 F and PM6:Y6 a,c) without QDs and b,d) with QDs. The calculated photogenerated exciton distribution in the different photoactive layers e,g) without QDs and f,h) with QDs.

the HH-CIS QDs and photoactive layer are higher than that at the interface between PDINN and photoactive layer in the control device.

3. Conclusions

In conclusion, the exquisitely prepared short-ligand hydroxyl-terminated HH-CIS core–shell QDs as the cathode interface modifier were introduced into the nonfullerene OSCs for the first time. The wide absorption range, and higher charge separation capability of HH-CIS QDs as compared with common QDs, is due to their type-II structure enabled by the unique heterophase homojunction which can enhance the sunlight harvesting and charge transport ability of nonfullerene OSCs. Meanwhile, the incorporation of small QDs onto the photoactive layer could effectively "smooth out" the defects on the upper photoactive layer and improving the interfacial contact between the photoactive layer and PDINN ETL and allowing better charge transfer and reduced charge recombination. Based on the abovementioned advantages of ME-HH-CIS QDs, significant enhancement of the PCEs was achieved for different devices by incorporating ME-HH-CIS QDs. The highest PCE of optimized devices approached 16.26%, which is the highest efficiency reported so far for eco-friendly QD-enhanced OSCs. Similarly, importantly, our specifically designed HH-CIS core–shell QDs and the way of their integration into OSCs demonstrate a good universality in increasing the photovoltaic performance of different types of OSC devices. This work verifies that it is a promising approach to construct higher efficiency nonfullerene OSCs by rationally designing and incorporating QDs.

4. Experimental Section

Chemicals: Copper(I) iodide (CuI, 98%), indium(III) acetate (In(CH$_3$COO)$_3$, 99.99%), thioacetamide (98%), *tert*-dodecanethiol (*t*-DDT, 98%), 1-dodecanethiol (1-DDT, 98%), oleylamine (OAm, 90%),

1-octadecene (ODE, 90%), toluene (99%, anhydrous), and ethanol (99.8%, anhydrous) were purchased from Sigma–Aldrich. Zinc acetate dihydrate (Zn(CH$_3$COO)$_2$·2H$_2$O, 99.9%), ethanolamine (NH$_2$CH$_2$CH$_2$OH, 99.5%), 2-methoxy ethanol (CH$_3$OCH$_2$CH$_2$OH, ME, 99.8%), 1,8-diiodooctane (DIO, 98%), lithium fluoride (LiF), and molybdenum trioxide interlayer (MoO$_3$) materials were obtained from Sigma–Aldrich. Poly[(2,6-(4,8-bis(5-(2-ethylhexyl-3-fluoro)thiophen-2-yl)-benzo[1,2-b:4,5-b']dithiophene))-alt-(5,5-(1',3'-di-2-thienyl-5',7'-bis(2-ethylhexyl)benzo[1',2'-c:4',5'-c']dithiophene-4,8-dione)] (PM6) polymer, 3,9-bis(2-methylene-((3-(1,1-dicyanomethylene)-6,7-difluoro)-indanone))-5,5,11,11-tetrakis(4-hexylphenyl)-dithieno[2,3-d:2',3'-d']-s-indaceno[1,2-b:5,6-b']dithiophene (ITIC-4 F) molecule, 2,2'-((2Z,2'Z)-((12,13-bis(2-ethylhexyl)-3,9-diundecyl-12,13-dihydro-[1,2,5] thiadiazolo[3,4-e]thieno[2″,3″:4',5']thieno[2',3':4,5]pyrrolo[3,2-g]thieno[2',3':4,5]thieno[3,2-b]indole-2,10-diyl)bis(methanylylidene))bis(5,6-difluoro-3-oxo-2,3-dihydro-1 H-indene-2,1-diylidene))dimalononitrile (Y6), N,N'-bis{3-[3-(dimethylamino)propylamino]propyl perylene-3,4,9,10-tetracarboxylic diimide (PDINN), poly(9,9-bis(3'-(N,N-dimethyl)-N-ethylammoinium-propyl-2,7-fluorene)-alt-2,7-(9,9-dioctyl-fluorene))dibromide (PFN-Br), and poly(3,4-ethylenedioxythiophene) polystyrene sulfonate (PEDOT:PSS) were purchased from 1-Material company (Canada). Patterned indium tin oxide (ITO) glass substrates ($R_s \leq 10\,\Omega\,\mathrm{sq}^{-1}$, $T_r \geq 83\%$) were purchased from Shenzhen Huayu Union Technology Co., Ltd. (China). All chemicals were used as received without further treatment.

Synthesis of HH-CIS QDs: Oil-dispersible HH-CIS QDs were synthesized according to a method modified from the one reported in the literature.[30] First, the thioacetamide/OAm solution was obtained by blending thioacetamide (150.2 mg, 2 mmol) and OAm (1 mL) to form a bright yellow solution. In a typical synthetic process, CuI (95 mg, 0.25 mmol), In(OAc)$_3$ (146 mg, 0.25 mmol), 1-DDT (2.5 mL), and ODE (2.5 mL) were loaded in a 50 mL three-necked round-bottomed flask and heated to 160 °C with stirring under vacuum for 10 min. Then the temperature of the reaction solution was dropped to 60 °C followed by injecting 0.5 mL of thioacetamide/OAm and then kept at this temperature for another 1 h. The core CIS QD dispersion was subsequently precipitated and centrifuged with excessive ethanol and acetone. The oil-dispersible core CIS QD precipitate was redispersed in 3.0 mL toluene. To obtain the HH-CIS QDs, CuI (47.6 mg, 0.125 mmol), In(OAc)$_3$ (73 mg, 0.125 mmol), OAm (2 mL), and OED (2 mL) were blended in a 50 mL three-necked flask and heated to 180 °C for 5 min. Then 1.0 mL core CIS QDs mixed with 0.5 mL *t*-DDT were injected into the above solution and maintained at 180 °C for another 30 min. The obtained HH-CIS QDs were purified by a subsequent dispersion in toluene and precipitation with

ethanol 3 times and finally dispersed in 5 mL of toluene. The shell thickness was tuned by controlling the volume ratio of core QDs and shell precursor dispersions.

Preparation of Hydroxyl-Terminated HH-CIS QDs: The alcohol-dispersible HH-CIS QDs capped by short-ligand ME were prepared via ligand exchange process.[46] Typically, 200 uL QDs ($\approx$35 mg mL^{-1}) were first dispersed into 200 uL toluene followed by the addition of 200 uL of ME under stirring. After 30 min, the obtained alcohol-soluble QDs were purified through precipitation with the addition of hexane and subsequent centrifugation. The purified ME-capped core–shell CIS QDs were finally redispersed in methanol for further use.

Fabrication of Nonfullerene OSCs: The nonfullerene OSCs devices were fabricated with the following configuration: ITO glass/PEDOT:PSS/PM6:ITIC-4F (Y6)/QDs/PDINN/Ag. The patterned ITO glass was under ultrasonic cleaning with deionized water, acetone, and isopropanol for 10 min at each step, and then treated with ozone for 10 min. The PEDOT:PSS solution was spin-coated on top of the ITO glass at 4000 rpm for 1 min and annealed at 170 °C for 10 min. Subsequently, the photoactive layer deposition solution consisting of PM6:ITIC-4F (1:1 w/w, 20 mg mL^{-1}) in chlorobenzene with 0.5% volume ratio of DIO additive was spin-coated on top of PEDOT:PSS at 3000 rpm for 1 min. Then the photoactive layer was annealed at 160 °C for 15 min. For PM6:Y6-based devices, the photoactive layer was spin-coated at 3000 rpm for 45 s from a solution of PM6:Y6 (1:1.2, w/w, 16 mg mL^{-1}) in chloroform with 0.5% volume ratio of DIO as additive. The photoactive layer was annealed at 110 °C for 10 min. A certain amount of ME-capped HH-CIS QDs solution was spin-coated on top of the photoactive layer at 5000 rpm for 1 min. After that, the PDINN (1 mg mL^{-1} in methanol), as a cathode buffer layer, was spin-coated on the surface of the photoactive layer at 3000 rpm for 30 s. When PFN-Br was used as interfacial layer, a solution of 0.5 mg mL^{-1} PFN-Br in methanol was spin-coated at 4000 rpm for 30 s. Finally, a layer of Ag (100 nm) was deposited by thermal evaporation as the top electrode. For the fabrication of the inverted OSCs, the ZnO precursor was first spin-coated on the top of ITO over glass at 4500 rpm for 60 s followed by sintering at 200 °C for 1 h in air. The ZnO precursor solution was obtained by mixing zinc acetate dehydrate with 2-methoxy ethanol and ethanolamine. Then, the photoactive layer of PM6:ITIC-4F was prepared by the above mentioned procedure. The MoO₃ HTL ($\approx$25 nm) and Ag electrode ($\approx$100 nm) were sequentially deposited on top of the surface of the photoactive layer by thermal evaporation in the vacuum chamber. The effective device area was 0.06 cm².

Characterization: The UV–vis absorption spectra of HH-CIS QDs were measured using a Varian Cary 5000 scan UV–vis–NIR spectrometer at room temperature. Steady-state photoluminescence (PL) and time-resolved PL (TRPL) spectra were obtained by a Horiba Jobin Yvon Fluorolog-3 fluorescence spectrometer. The excitation wavelength was 375 nm. PL lifetimes were calculated by fitting the TRPL decay curves with a biexponential fitting equation. Transmission electron microscopy (TEM) images of HH-CIS QDs were obtained through a JEOL JEM-2100 microscope working at an accelerating voltage of 200 kV. Fourier transform infrared (FTIR) spectra of the prepared samples were recorded on a Thermo Scientific 4700 FTIR spectrometer. A VG Escalab 220i-XL X-ray photoelectron spectroscopy (XPS) equipped with a twin anode Al Kα radiation X-ray source was used to analyze the chemical composition of the samples. The crystal structures of all the samples were analyzed by the X-ray diffraction instrument (XRD, PANalytical X'Pert MRD) with a Cu Kα radiation source ($\lambda = 0.15406$ nm) operated at 45 kV and 40 mA. Ultraviolet photoelectron spectroscopy (UPS) measurements were carried out with an unfiltered Helium gas discharge lamp emitting predominantly at 21.22 eV to determine the work function of the photoactive film materials with deposited QDs. Neutron activation analysis (NAA) measurements were performed using a SLOWPOKE nuclear reactor to determine the concentration of QDs on the surface of the photoactive layer. The film morphology of the photoactive layer was studied by atomic force microscopy (AFM, Bruker, MultiMode 8) operating with the ScanAsyst mode. The current density–voltage (*J*–*V*) curves of OSCs were measured by a Keithley 2400 source meter illuminated under AM1.5 G spectrum from a solar simulator (Oriel, Model No. 94022A). Light intensity was calibrated to

100 mW cm^{-2} by using an NREL Si solar reference cell. A photoactive area of 0.06 cm² was defined by a black metal mask. External quantum efficiency (EQE) curves were carried out on a Keithley 2000 multimeter under the illumination of a 300 W tungsten lamp with a Spectral DK240 monochromator. The carrier mobility was measured by applying the space charge limited current (SCLC) method. The hole-only device structure was ITO/PEDOT:PSS/ photoactive layer/QDs/MoO₃/Ag, and the device structure for electron-only device was ITO/ZnO/photoactive layer/QDs/PDINN/Ag.

Supporting Information

Supporting Information is available from the Wiley Online Library or from the author.

Conflict of Interest

The authors declare no conflict of interest.

Data Availability Statement

The data that support the findings of this study are available from the corresponding author upon reasonable request.

[1] L. Zhu, M. Zhang, J. Xu, C. Li, J. Yan, G. Zhou, W. Zhong, T. Hao, J. Song, X. Xue, Z. Zhou, R. Zeng, H. Zhu, C. Chen, R. Mackenzie, Y. Zou, J. Nelson, Y. Zhang, Y. Sun, F. Liu, *Nat. Mater.* **2022**, *21*, 656.

[2] T. Yu, W. He, M. Jafari, T. Guner, P. Li, M. Siaj, R. Izquierdo, B. Sun, G. C. Welch, A. Yurtsever, D. Ma, *Small Methods* **2022**, *6*, 2100916.

[3] M. Chen, J. Wang, F. Yin, Z. Du, L. A. Belfiore, J. Tang, *J. Mater. Chem. A* **2021**, *9*, 4505.

[4] F. P. G. D. Arquer, D. V. Talapin, V. I. Klimov, Y. Arakawa, M. Bayer, E. H. Sargent, *Science* **2021**, *373*, 8541.

[5] Y. W. Han, E. J. Lee, J. Joo, J. Park, T. H. Sung, D. K. Moon, *J. Mater. Chem. A* **2016**, *4*, 10444.

[6] R. Peng, T. Yan, J. Chen, S. Yang, Z. Ge, M. Wang, *Adv. Electron. Mater.* **2020**, *6*, 1901245.

[7] L. Tan, F. Yang, M. R. Kim, P. Li, D. T. Gangadharan, J. Margot, R. Izquierdo, M. Chaker, D. Ma, *ACS Appl. Mater. Interfaces* **2017**, *9*, 26257.

[8] L. Wu, J. Huang, Y. Xie, L. Hong, R. Peng, W. Song, L. Huang, L. Zhu, W. Bi, Z. Ge, *Sol. RRL* **2019**, *3*, 1900117.

[9] S.-W. Baek, S. Jun, B. Kim, A. H. Proppe, O. Ouellette, O. Voznyy, C. Kim, J. Kim, G. Walters, J. H. Song, S. Jeong, H. R. Byun, M. S. Jeong, S. Hoogland, F. P. García de Arquer, S. O. Kelley, J.-Y. Lee, E. H. Sargent, *Nat. Energy* **2019**, *4*, 969.

[10] N. Guijarro, L. Yao, F. Le Formal, R. A. Wells, Y. Liu, B. P. Darwich, L. Navratilova, H. H. Cho, J. H. Yum, K. Sivula, *Angew. Chem., Int. Ed.* **2019**, *58*, 12696.

[11] Y. W. Han, S. J. Jeon, J. Y. Choi, J. H. Kim, D. K. Moon, *Sol. RRL* **2018**, *2*, 1800077.

[12] Z. Li, X. Zhang, C. Liu, Z. Zhang, Y. He, J. Li, L. Shen, W. Guo, S. Ruan, *J. Phys. Chem. C* **2015**, *119*, 26747.

[13] Y. Wang, B. Jia, J. Wang, P. Xue, Y. Xiao, T. Li, J. Wang, H. Lu, Z. Tang, X. Lu, F. Huang, X. Zhan, *Adv. Mater.* **2020**, *32*, 2002066.

[14] R. Soltani, A. A. Katbab, K. Schaumberger, N. Gasparini, C. J. Brabec, S. Rechberger, E. Spiecker, A. G. Alabau, A. Ruland, A. Saha, D. M. Guldi, V. Sgobba, T. Ameri, *J. Mater. Chem. C* **2017**, *5*, 654.

[15] Y. Park, S. Y. Bae, T. Kim, S. Park, J. T. Oh, D. Shin, M. Choi, H. Kim, B. Kim, D. C. Lee, J. H. Song, H. Choi, S. Jeong, Y. Kim, *Adv. Energy Mater.* **2022**, *12*, 2104018.

[16] G.-H. Lim, K. S. Lee, Y. J. Park, J. Shim, J. W. Choi, M. Kim, Y. Jin, B. Lim, Y. Yi, C.-L. Lee, J. Y. Hwang, D. I. Son, *J. Mater. Chem. C* **2019**, *7*, 11797.

[17] B. J. Moon, S. Cho, K. S. Lee, S. Bae, S. Lee, J. Y. Hwang, B. Angadi, Y. Yi, M. Park, D. I. Son, *Adv. Energy Mater.* **2015**, *5*, 1401130.

[18] D. Scheunemann, S. Wilken, J. Parisi, H. Borchert, *Phys. Chem. Chem. Phys.* **2016**, *18*, 16258.

[19] Y. Wang, J. Li, T. Li, J. Wang, K. Liu, Q. Jiang, J. Tang, X. Zhan, *Small* **2019**, *15*, 1903977.

[20] X. Zhang, Q. Jiang, J. Wang, J. Tang, *Sol. Energy* **2020**, *206*, 670.

[21] C. Kim, I. Kozakci, J. Kim, S. Y. Lee, J. Y. Lee, *Adv. Energy Mater.* **2022**, *12*, 2200262.

[22] S. Jiao, Q. Shen, I. Mora-Sero, J. Wang, Z. Pan, K. Zhao, Y. Kuga, X. Zhong, J. Bisquert, *ACS Nano* **2015**, *9*, 908.

[23] J. Wang, I. Mora-Seró, Z. Pan, K. Zhao, H. Zhang, Y. Feng, G. Yang, X. Zhong, J. Bisquert, *J. Am. Chem. Soc.* **2013**, *135*, 15913.

[24] S. J. Lim, A. Schleife, A. M. Smith, *Nat. Commun.* **2017**, *8*, 14849.

[25] B. Mahler, N. Lequeux, B. Dubertret, *J. Am. Chem. Soc.* **2010**, *132*, 953.

[26] Y. Ghosh, B. D. Mangum, J. L. Casson, D. J. Williams, H. Htoon, J. A. Hollingsworth, *J. Am. Chem. Soc.* **2012**, *134*, 9634.

[27] X. Ruan, X. Cui, Y. Cui, X. Fan, Z. Li, T. Xie, K. Ba, G. Jia, H. Zhang, L. Zhang, W. Zhang, X. Zhao, J. Leng, S. Jin, D. J. Singh, W. Zheng, *Adv. Energy Mater.* **2022**, *12*, 2200298.

[28] P. Cui, D. Wei, J. Ji, H. Huang, E. Jia, S. Dou, T. Wang, W. Wang, M. Li, *Nat. Energy* **2019**, *4*, 150.

[29] H. Guo, B. Luo, J. Wang, B. Wang, X. Huang, J. Yang, W. Gong, Y. Zhou, X. Niu, *J. Mater. Chem. A* **2020**, *8*, 24655.

[30] J. Ning, S. V. Kershaw, A. L. Rogach, *J. Am. Chem. Soc.* **2019**, *141*, 20516.

[31] J. Ning, Y. Xiong, F. Huang, Z. Duan, S. V. Kershaw, A. L. Rogach, *Chem. Mater.* **2020**, *32*, 7842.

[32] J. Bang, J. Park, J. H. Lee, N. Won, J. Nam, J. Lim, B. Y. Chang, H. J. Lee, B. Chon, J. Shin, J. B. Park, J. H. Choi, K. Cho, S. M. Park, T. Joo, S. Kim, *Chem. Mater.* **2010**, *22*, 233.

[33] S. A. Ivanov, A. Piryatinski, J. Nanda, S. Tretiak, K. R. Zavadil, W. O. Wallace, D. Werder, V. I. Klimov, *J. Am. Chem. Soc.* **2007**, *129*, 11708.

[34] O. Almora, C. I. Cabrera, J. Garcia-Cerrillo, T. Kirchartz, U. Rau, C. J. Brabec. *Adv. Energy Mater.* **2021**, *11*, 2100022.

[35] J. Yao, B. Qiu, Z.-G. Zhang, L. Xue, R. Wang, C. Zhang, S. Chen, Q. Zhou, C. Sun, C. Yang, M. Xiao, L. Meng, Y. Li, *Nat. Commun.* **2020**, *11*, 2726.

[36] M.-H. Jao, H.-C. Liao, W.-F. Su, *J. Mater. Chem. A* **2016**, *4*, 5784.

[37] R. Sharma, H. Lee, M. Seifrid, V. Gupta, G. C. Bazan, S. Yoo, *Sol. Energy* **2020**, *201*, 499.

[38] M. B. Upama, N. K. Elumalai, M. A. Mahmud, M. Wright, D. Wang, C. Xu, A. Uddin, *Sol. Energy Mater Sol. Cells* **2018**, *176*, 109.

[39] W. Li, J. Cai, Y. Yan, F. Cai, S. Li, R. S. Gurney, D. Liu, J. D. McGettrick, T. M. Watson, Z. Li, A. J. Pearson, D. G. Lidzey, J. Hou, T. Wang, *Sol. RRL* **2018**, *2*, 1800114.

[40] A. Pockett, H. Lee, B. L. Coles, W. C. Tsoi, M. J. Carnie, *Nanoscale* **2019**, *11*, 10872

[41] R. C. I. MacKenzie, C. G. Shuttle, G. F. Dibb, N. Treat, E. V. Hauff, M. J. Robb, C. J. Hawker, M. L. Chabinyc, J. Nelson, *J. Phys. Chem. C* **2013**, *117*, 12407.

[42] R. Hanfland, M. A. Fischer, W. Brütting, U. Würfel, R. C. I. MacKenzie, *Appl. Phys. Lett.* **2013**, *103*, 063904.

[43] B. J. Tremolet de Villers, R. C. I. MacKenzie, J. J. Jasieniak, N. D. Treat, M. L. Chabinyc, *Adv. Energy Mater.* **2014**, *4*, 1301290.

[44] R. Kerremans, C. Kaiser, W. Li, N. Zarrabi, P. Meredith, A. Armin, *Adv. Opt. Mater.* **2020**, *8*, 2000319.

[45] M. I. Alonso, K. Wakita, J. Pascual, M. Garriga, N. Yamamoto, *Phys. Rev. B*, **2001**, *63*, 075203.

[46] Z. Bai, W. Ji, D. Han, L. Chen, B. Chen, H. Shen, B. Zou, H. Zhong, *Chem. Mater.* **2016**, *28*, 1085.